Title: Probability-based mechanisms in biological networks with parameter uncertainty.

Authors: Oscar O. Ortega[1], Blake A. Wilson[2], James C. Pino[2], Michael W. Irvin[2], Geena V. Ildefonso[1], Shawn P. Garbett[3], Carlos F. Lopez[2,4*]

Abstract:

Mathematical models of biomolecular networks are commonly used to study mechanisms of cellular processes, but their usefulness is often questioned due to parameter uncertainty. Here, we employ Bayesian parameter inference and dynamic network analysis to study dominant reaction fluxes in models of extrinsic apoptosis. Although a simplified model yields thousands of parameter vectors with equally good fits to data, execution modes based on reaction fluxes clusters to three dominant execution modes. A larger model with increased parameter uncertainty shows that signal flow is constrained to eleven execution modes that use 53 out of 2067 possible signal subnetworks. Each execution mode exhibits different behaviors to *in silico* perturbations, due to different signal execution mechanisms. Machine learning identifies informative parameters to guide experimental validation. Our work introduces a probability-based paradigm of signaling mechanisms, highlights systems-level interactions that modulate signal flow, and provides a methodology to understand mechanistic model predictions with uncertain parameters.

Affiliations:

1. Chemical and Physical Biology Program, Vanderbilt University, Nashville, TN 37212
2. Dept. of Biochemistry, Vanderbilt University, Nashville, TN 37212
3. Dept. of Biostatistics, Vanderbilt University Medical Center, Nashville, TN 37203
4. Dept. of Biomedical Informatics, Vanderbilt University Medical Center, Nashville, TN 37203

Introduction

Many biological processes can be represented as networks of interconnected biochemical components enabling the study of their dynamics and signaling mechanisms (Jordan, Landau and Iyengar, 2000; Bonneau, 2008; Janes, Reinhardt and Yaffe, 2008; Weerts, Van den Hof and Dankers, 2018). These analyses typically entail building a network, either from prior knowledge or through network inference, developing a mathematical model of the network interactions, and subsequently calibrating the model to experimental data (Jaqaman and Danuser, 2006; Raue *et al.*, 2011; Shockley, Vrugt and Lopez, 2018). Although small networks have been studied with great success, the fact remains that for large networks many parameters remain difficult to ascertain and optimization routines yield multiple parameter sets that reproduce the protein concentration trajectories equally well (Ryan N. Gutenkunst *et al.*, 2007; Eydgahi *et al.*, 2013; Mitra and Hlavacek, 2019). This has led to a common practice whereby one or a few parameter vectors are chosen to make mechanistic predictions which can be validated by experiments with varying degrees of success (Janes *et al.*, 2005; Albeck *et al.*, 2008; Becker *et al.*, 2010). However, criticisms remain regarding the usefulness of large and complex mathematical models of cellular processes with many uncertain parameters.

Information Theory based methods (Shannon, 1948) have been one of the successful approaches to date to explain input/output responses of intracellular signaling pathways (Cheong *et al.*, 2011; Brennan, Cheong and Levchenko, 2012; Levchenko and Nemenman, 2014; Suderman *et al.*, 2017; Shockley *et al.*, 2019). These approaches cast signal transduction in terms of channel capacities – the maximum amount of biochemical information that can travel from an input stimulus to an output response. These analyses have revealed that the maximum channel capacity of a biochemical process is context dependent and could require the cooperativity of multiple cells to achieve actual information transfer (Suderman *et al.*, 2017). Previous work also applied information theoretic analysis to an allosterically regulated network and observed that the preferred path for information flow through the network was highly dependent on substrate concentrations (Shockley *et al.*, 2019). Although these insights have been valuable to advance our understanding cellular regulatory processes, questions still remain about how reaction rates from non-equilibrium dynamics modulate signal flow in a biochemical network and further how these transient dynamics are impacted by parameter uncertainty.

Analysis of execution patterns in biochemical networks necessarily implies a detailed understanding of instantaneous fluxes throughout the system. However, reaction-flux based analysis is particularly challenging due to multiple concurrent biochemical interactions and their associated reaction rate fluctuations in time (Nobeli, Favia and Thornton, 2009). Therefore, the number of interactions and temporal dynamics makes it difficult to establish whether persistent behaviors emerge from myriad biochemical reactions. Recent works in Tropical Geometry and Ultradiscretization Theory have proposed a mathematical formalism that makes it possible to map continuous functions into piecewise linear meshes in the Ultradiscrete space (Kato, Tsujimoto and Zuk, 2017a). Approaches inspired in these novel mathematical treatments have been used to guide biochemical model reduction and simplification (Noel, Grigoriev and

Vakulenko, 2011). For this work, we hypothesized dynamic analysis using these methods could enable us to identify dominant fluxes in a dynamic biochemical network, identify patterns of execution, and explore their dependence on model parameters. We reasoned that we could cast this analysis onto a Bayesian probability framework to assign statistical weight to the identified execution patterns, thus providing a novel statistical interpretation to cellular reaction mechanisms.

The remainder of the article is organized as follows. We first show how Bayesian inference of model parameters can yield tens of thousands of parameter vectors that all reproduce an experimental data set equally well. We then introduce a method, inspired in Ultradiscretization Theory and Tropical Algebra, to define a dynamic signal execution fingerprint, which can then be used to cluster execution modes according to model parameters. Surprisingly, we find that despite the thousands of parameter vectors that fit the experimental data of a biological system, only a handful of execution modes emerge as possible signal processing mechanisms. Subsequently, we demonstrate how parameter vectors that belong to different execution modes offer a biased view of signaling processes that could easily lead to misleading interpretations of network-driven processes. We further demonstrate how increases in parameter unidentifiability exacerbate the problem of model certainty in signal execution, but still identify the signal execution path probabilities associated with a given set of parameters. Our work therefore shows that network dynamics exploration, given available experimental data, could play a central role to identify true systems-level processes that shed light on signal processing mechanisms from a statistical perspective.

Results

Bayesian parameter optimization yields indistinguishable protein concentration dynamics.

To investigate the role of parameter uncertainty on signal execution through biochemical networks we focused on the extrinsic apoptosis form of programmed cell death (Elmore, 2007). Apoptosis is a ubiquitous biological process in metazoans used as a mechanism to maintain cell numbers and overall organism homeostasis (Koonin and Aravind, 2002). For the first part of our analysis we employed a modified version of the Extrinsic Apoptosis Reaction Model (EARMv2.0) (Lopez *et al.*, 2013). We found this abridged EARM (aEARM), depicted in Figure 1A, was the largest model we could build that would both preserve key biochemical interactions that represent extrinsic apoptosis, and in which all model parameters achieve convergence by the Gelman-Rubin diagnostics after parameter calibration with Bayesian methods. The model captures key biological features of apoptosis execution including signal initiation by TNF-Related Apoptosis Inducing Ligand (TRAIL), subsequent activation of initiator caspases (Caspase 8) (Kantari and Walczak, 2011) type 1 and type 2 activation of effector caspases (Caspase 3) (Özören and El-Deiry, 2002) and completion of apoptosis execution by cleavage of Poly(ADP-ribose) polymerase (PARP) (Kaufmann *et al.*, 1993). Overall, aEARM comprises 22 molecular species and 34 kinetic parameters (see details in Methods). We used PyDREAM (Shockley, Vrugt and Lopez, 2018) to calibrate the model to previously published experimental data that comprises the concentration dynamics of truncated Bid (tBid) and cleaved PARP (cPARP). Given

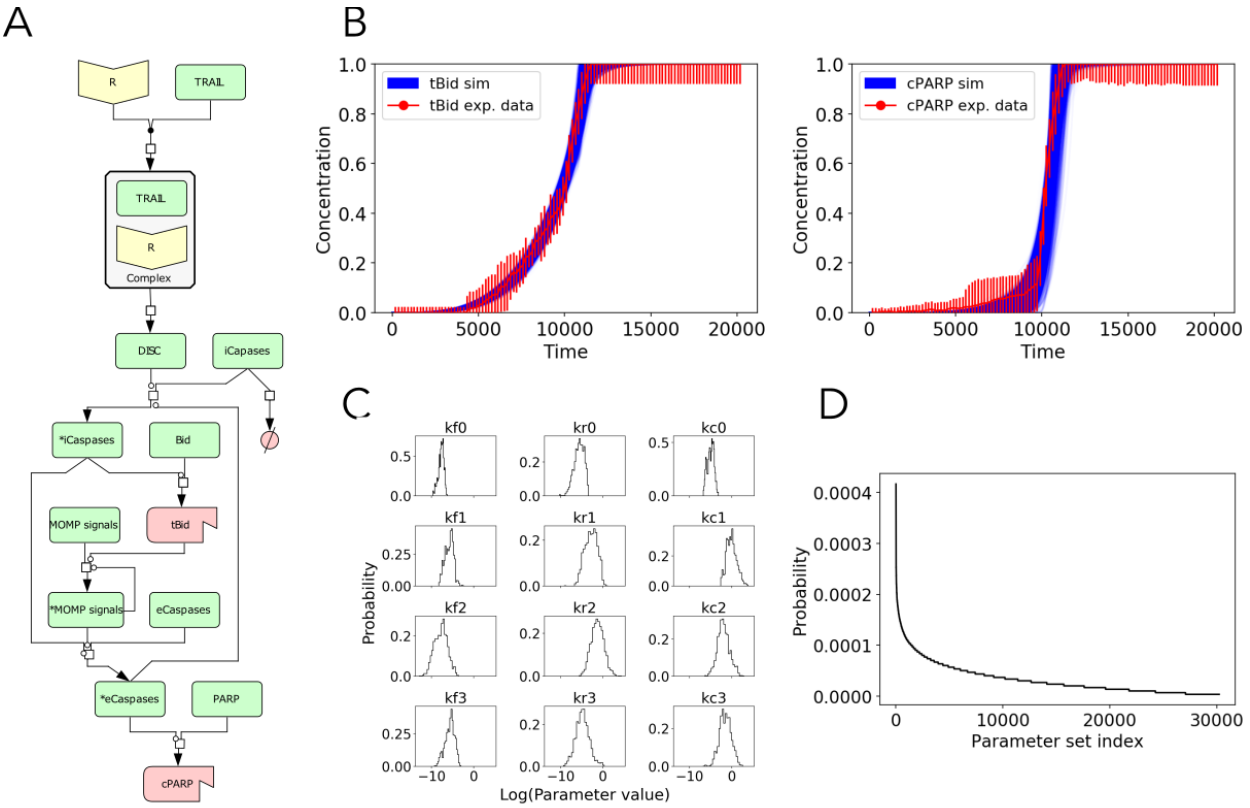

Figure 1. Abridged Extrinsic Apoptosis Reaction (aEARM) network and parameter calibration results. A) Reaction network using the Kitano convention. Yellow nodes are protein receptors, green nodes are generic proteins, and red nodes are truncated/cleaved proteins. B) Simulated trajectories of truncated Bid and Cleaved PARP calibrated to reproduce the experimental data. Red dots and bars indicate the mean and standard deviation of the experimental data and blue lines correspond to the simulated trajectories. C) Marginal probability distributions of the first 12 individual kinetic parameters that were recovered from the PyDREAM run by integrating out all other dimensions. Forward rates, reverse rate, and catalytic values were all found to be within biologically relevant ranges (Zhou, 2010)*. D) Probability of each of the unique parameter vectors sampled after burn-in in the PyDREAM calibration. To obtain the probability of each parameter set the number of visits to a specific parameter vector was normalized by the total number of visits.*

that the model was calibrated to HeLa cell data, we hypothesize that signal patterns are representative of signal processing and execution of Type-II cells treated with death-inducing ligands such as TRAIL. In all, we ran the PyDREAM sampling for 100,000 steps after burn-in and collected 300,000 parameter vectors from which 27,242 were unique. All unique parameter vectors fit the data equally well (Figure 1B). All parameters were deemed to have converged by the Gelman-Rubin diagnostics as shown in Supplemental Table 1 and Supplemental Figure 2 (Gelman and Rubin, 1992). We obtained the marginal distributions from the sampled parameter vectors as show in Figure 1C and Supplemental Figure 3. Given the Markov Chain Monte Carlo (MCMC) aspect of our parameter inference method, we were able to obtain parameter vector probabilities as shown in Figure 1D (Chiband and Greenberg, 2008). The probability distribution of parameter vectors exhibits characteristic exponential-like decay shape indicating that some parameters are more likely than others. With this calibrated model to experimental data, we then probed signal execution patterns in the aEARM network from a probabilistic perspective. We note that throughout the manuscript, a parameter vector refers to a set of positive real values, one value for each of the kinetic parameters defined in aEARM,

used to run a simulation. A parameter distribution refers to the frequency of occurrence of different values from the same kinetic parameter.

A discretized flux-based analysis of signal execution in networks.

As shown in Figure 1B, all the parameter vectors obtained from the Bayesian calibration yield protein concentration dynamics indistinguishable from the experimental trajectories of tBid and cPARP. Individual parameters from these vectors take widely different values as depicted by their distributions in Figure 1C. This uncertainty in the parameter values affects the reaction rates of the protein interactions generating different reaction flux patterns in the network during signal execution. We therefore wanted to study the non-equilibrium flux of the reactions in the aEARM network and aimed to explore whether parameter uncertainty yielded specific patterns of signal execution.

Analysis of flux dynamics during signal execution requires tracking the signal flow through a network at all simulation time points as multiple concurrent reaction rates consume or produce molecular species. We assumed that the reactions with the highest flux at any given time dominate the network signal execution and provide a proxy to observe the effect of different parameter vectors in the network. Our aim was thus to identify the reaction rates with the highest flux throughout the whole network as simulations evolved over time. To analyze the non-equilibrium flux and find the dominant reaction paths during signal execution, we developed an algorithm inspired by Ultradiscretization Theory and Tropical Algebra as described in *Methods* (Noel, Grigoriev and Vakulenko, 2011; Kato, Tsujimoto and Zuk, 2017b). Our approach enabled us to identify paths relevant for flux propagation in non-equilibrium states. We refer to these paths of flux propagation through the network as *execution modes* for the remainder of this manuscript.

We introduce the workflow for reaction flux discretization and execution mode identification as shown schematically in Figure 2A-B. Signal discretization requires three steps. First, we identify a target node (Fig 2B) for which the signal flux will be tracked. Second, we calculate the reaction rates that produce or consume the target node, identify the largest reaction rate (x) and test whether it is dominant over other reactions (y) using the discretization operation $|\log_{10} x| - |\log_{10} y| > \rho$, where ρ is the order of magnitude difference necessary to consider dominance (see Methods section for details). Third, we identify the chemical species produced by the dominant reaction(s) and jump to that species, thus starting the process again from the first step, and thereby tracking the dominant signal fluxes through the whole network and obtaining a subnetwork. This dominant subnetwork is assigned a unique integer label as shown in Figure 2A. The procedure is repeated for all simulation time points. As a result, the dynamic nature of signal execution for a given parameter vector is abstracted to a sequence of labels that can be compared to other sequences using a suitable metric (Figure 2B). We call this sequence of labels obtained from a simulation a *dynamic fingerprint* because it is unique for a given signal processing event with a specific parameter set. A workflow of the algorithm is shown in Supplemental Figure 1

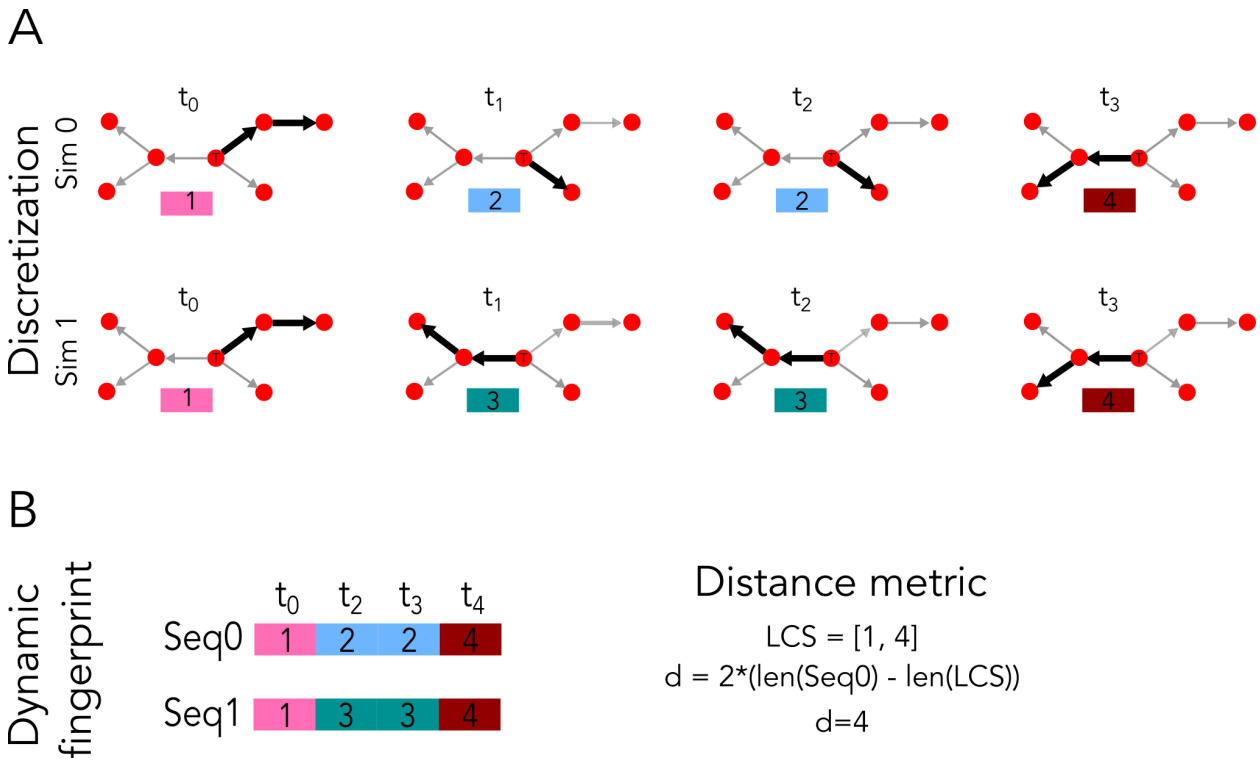

Figure 2. PyDyno workflow. A) First, the network of interaction is obtained from a model and a target node (labeled T) from where the signal is going to be tracked is defined. Red nodes are molecular species in a model, edges represent interactions between nodes, bolded edges are the dominant interactions. Next, at each time point of a simulation our analysis obtains a dominant subnetwork, bolded edges in the network, through which most of the signal is going through and this subnetwork is assigned a label. Sim 0 and Sim 1, simulations ran with different parameter sets, exhibit different dominant subnetworks. B) As each subnetwork is assigned a label, we can get a sequence of labels per simulation that can be compared to other simulations with the Longest Common Subsequence metric and obtain a distance matrix. This distance matrix can be used with clustering algorithms to obtain groups with similar modes of signal execution.

Key execution modes emerge despite parameter uncertainty

To identify the dynamic execution patterns in aEARM in response to death ligand cues, we carried out our signal discretization analysis for the 27,242 unique parameters and obtained dynamic fingerprints for each parameter vector. We then asked whether there were similarities among dynamic fingerprints across parameter sets. To investigate this question, we quantified the distance between each dynamic fingerprint using the Longest Common Subsequence (LCS) metric. We chose this metric due to its sensitivity to order differences in which successive subnetworks labels appear (Studer and Ritschard, 2015). This metric thus assigns a larger distance to a pair of dynamics fingerprints that execute the signal differently. Next, we calculated the pairwise distance between all dynamic fingerprints obtaining a 27,242 by 27,242 distance matrix. This matrix enabled us to use an agglomerative clustering algorithm (Rokach and Maimon, 2005) to probe whether clusters of dynamic fingerprints would emerge. As shown in Figure 3A, we found that all 27,242 dynamic fingerprints could all be classified into three clusters (Supplemental Table 2), which we denominate “execution modes”. Given that each parameter vector has a defined probability (Figure 1D) and is associated with a dynamic fingerprint, we could calculate the probabilities of signal execution through each mode as 42%,

36%, and 22% for Execution Mode 1 (EM1), Execution Mode 2 (EM2), and Execution Mode 3 (EM3) respectively. These three execution modes account for all the parameter vectors inferred from the explored probability space and no vectors were found that did not belong to either of these modes. We note that these execution modes are comprise three subnetworks out of eight possible subnetworks for signal flow.

The dominant flux subnetwork for each execution mode is shown schematically in Figure 3B. We note the highlighted paths represent the dominant reaction fluxes, i.e. these fluxes are within an order of magnitude of the largest reaction at each node for the given parameter set and simulation time point. As shown, Execution Mode 1 (EM1) comprises events from initial death-ligand binding to the receptor, through formation of the Death Inducing Signaling Complex (DISC), and subsequent activation of initiator Caspase. The initiator Caspase then truncates and activates Bid, which in turn activates MOMP, a species that abstracts mitochondrial outer membrane pore (MOMP) formation. Activated MOMP can then further activate MOMP in a positive feedback loop and activate the effector Caspase downstream. As highlighted in Figure 3B(EM1), activated MOMP is dominantly used to both activate more MOMP, through the positive feedback loop, and activate the effector Caspase.

The flux through the network in Execution Mode 2 (EM2) is similar to that of Mode 1 but the execution path differs at MOMP regulation. As highlighted in blue in Figure 3B EM2, activated MOMP is largely consumed in the positive feedback loop to activate more MOMP. The signal flux downstream of activated MOMP is at least an order of magnitude less than the highlighted route for the parameters in EM2. Therefore, effector Caspase activation and apoptosis execution takes place due to a smaller reaction flux in the network relative to the MOMP-level activity in EM2. For those parameters belonging to EM3, signal execution seems to flow largely toward PARP cleavage, with less MOMP-level regulation. Our results therefore show that despite uncertainties in inferred model parameters due to limited available data, the modes of signal execution are identifiable. Identifying a limited number of execution modes highlights the need to thoroughly characterize the model parameter space, given experimental constraints, to understand and make inferences about execution mechanisms. We note that using a single vector of parameters would lead to incomplete model prediction as no one single parameter vector captures the rich dynamics exhibited by all the statistically inferred parameter vectors.

To further understand the impact of each execution mode on MOMP regulation, we examined the relative concentration of activated MOMP (MOMP*) and the binding complexes in which it participates. We calculated the percentages of MOMP*, inactive MOMP bound to MOMP* (MOMP-MOMP*), and effector caspase bound to MOMP* (EC-MOMP*). As shown in Figure 3C, the relative abundance of these species over time exhibits different concentration patterns in each execution mode. In EM1, the relative abundance of EC-MOMP* is ~20%, indicating that the signal flow through this reaction is lower than in EM3 but still important in the overall dynamics. In EM2, 85 % of MOMP* is bound to inactive MOMP at all time points before cell death. This can be explained by a high MOMP activation rate due to Bid and the MOMP* positive feedback loop autoactivation. In contrast to EM2, the MOMP-MOMP* abundance in EM3 decreased to ~35%, while EC-MOMP* is increased to ~50%. This increase in EC-MOMP*

abundance, indicates that the binding rate of MOMP* to EC is larger than the binding rate of MOMP to MOMP*. We note that the initial concentration of inactive MOMP in the model is an order of magnitude larger than that of EC. Thus, this result is in stark contrast with the result from EM2 where the reaction rates exhibit different relative values.

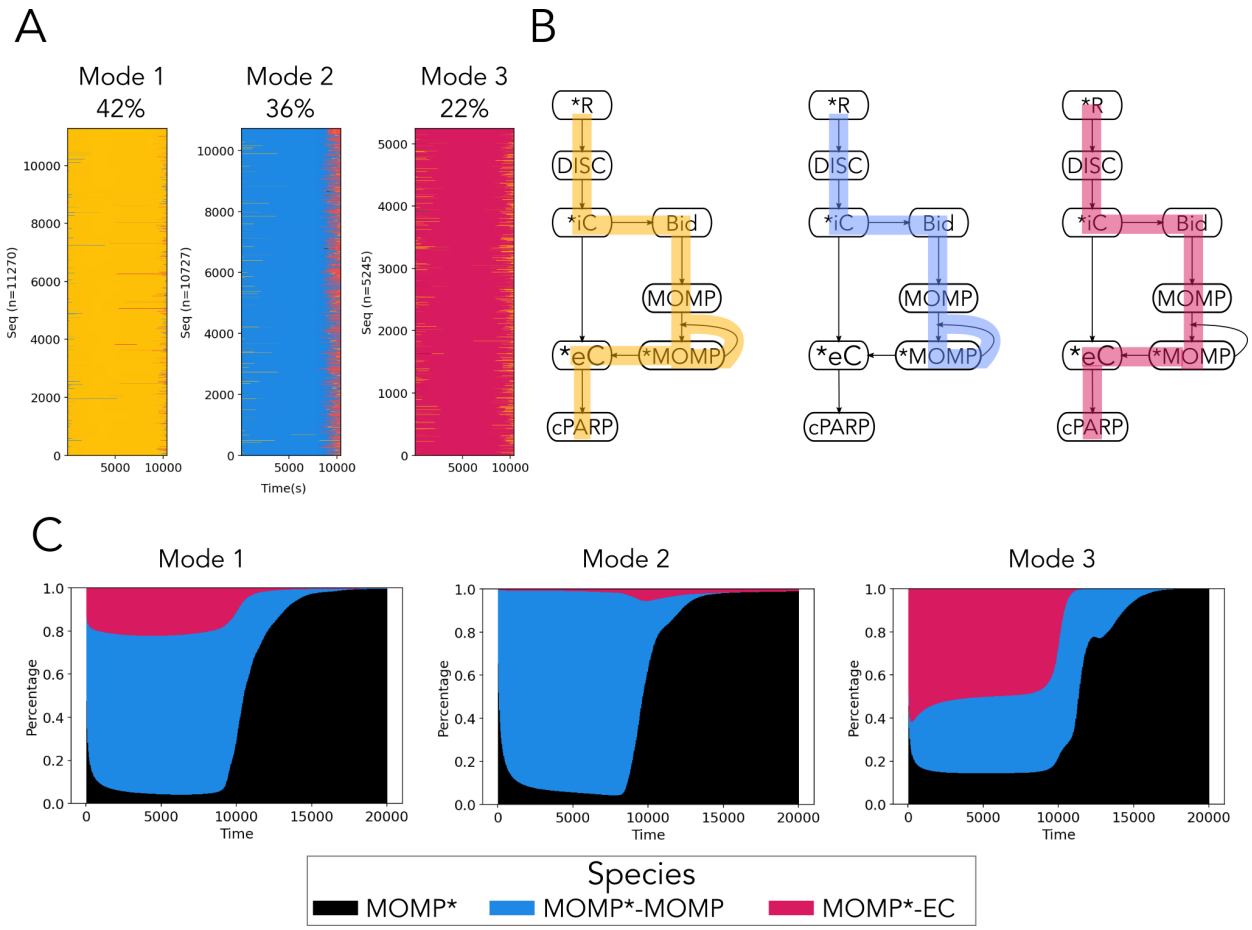

Figure 3. Modes of signal execution in aEARM. A) Dynamic fingerprints organized by the clusters they belong to. Each cluster plot is composed of horizontal lines that correspond to dynamic fingerprints, i.e. sequences of dominant subnetworks, and each subnetwork is assigned a different color. B) Signal execution modes as defined by the most common subnetwork in each cluster. The complete aEARM network is shown in black, and the dominant subnetworks for Mode 1, 2, and 3 are highlighted in yellow, blue, and red, respectively. C) Effect of the different signal execution modes in the relative concentration of activated MOMP and its associated complexes. For each cluster, we calculated the temporal relative concentration of MOMP, MOM*P-MOMP and MOMP*-EC point by obtaining their individual average concentrations and dividing it by the sum of their concentrations. This visualization provides insights about the usage MOMP* in each cluster.*

Signal execution modes respond differently to eCaspase perturbation

We then asked whether in-silico experiments could help us understand differences in signal execution that could lead to experimentally testable hypotheses. We therefore carried out *in-silico* knockdown experiments of eCaspase, as its activation is essential for the final steps of apoptosis execution (Mehal, Inayat and Flavell, 2006). In addition, effector caspase inhibitors are readily available for laboratory use (Perry *et al.*, 1997; Solania, González-Paéz and Wolan, 2019). We hypothesized that each execution mode would exhibit different execution

mechanisms when eCaspase was knocked down by 50%. To explore the impact of eCaspase knockdown for each execution mode, we compared the concentration dynamics for MOMP and cPARP given by wild type and eCaspase knockdown conditions.

For each execution mode we plotted the cPARP concentration trajectories and obtained the time of death (ToD) for each simulated cell as described in Methods. As shown in Figure 4A, the ToD in EM1 exhibits a modest decrease of 14.96 s, but also presents a larger standard deviation of 702 s. For EM 2 the ToD increased from 10351 $\pm$ 132 s (WT) to 10809 $\pm$ 226 s for eCaspase knockdown (Δt = 458 s). In contrast, EM3 eCaspase knockdown leads to a decreased ToD from 10261 $\pm$ 83 in WT to 9507 $\pm$ 516 s in the knockdown (Δt = -754 $\pm$ 523 s). These results therefore show that each execution mode can exhibit significantly different – and a times juxtaposed – responses to the same perturbation.

We then probed the effect of the eCaspase knockdown on the reaction rates associated to MOMP* (a node where the signal bifurcates): MOMP* binding to MOMP, and MOMP* binding to EC. Specifically, we focused on the reaction rate peak and the time to reach peak of the reaction rate throughout the simulation, as shown in Figure 4B and supplementary Figure 2. The peaks of the MOMP*+MOMP binding reaction (Figure 4B upper row) appear unchanged across all execution modes, yet the time to reach the peaks vary significantly. The median time to peaks were 6.14%, 0.36%, and 11.76% faster for modes 1, 2, and 3, respectively. Concurrently, the peaks of the MOMP*+EC binding reaction (Figure 4B lower row) are reduced approximately 50% as expected by the 50% reduction of the available EC, and the median time to peaks were 6.77%, 0.4%, and 14.48% faster for modes 1, 2, and 3, respectively. In combination, for mode 1, the relative change of the MOMP and EC reaction peaks have large interquartile ranges IQR= -10.37% to –1.01% and IQR=-1.13% to –11.39%, respectively, which explains the variability in the time to cell death. For mode 2, the time to the peak of MOMP and EC reactions change marginally and given that the EC peak is 50% of the WT condition, this leads to longer times to accumulate the necessary number of EC molecules for cells to commit to apoptosis. Finally, for mode 3, the median time to reach the MOMP reaction peak and the EC reaction peak is 11.76% and 14.48%, faster than in the WT condition, respectively. This causes faster activation of MOMP and EC which leads to earlier apoptosis in cells. To summarize, although the biochemical signal flows differently in each execution mode, the protein concentration dynamics exhibit similar outcomes (Figure 4A Wild Type). However, when a perturbation is made to the network, the outcome can vary significantly, as shown for each execution mode.

Reducing execution mode uncertainty through parameter measurements

Given that the aEARM calibrated parameter vectors yield three execution modes with their respective probabilities, there is uncertainty about which execution mode is most representative of the cellular process. We then asked whether we could identify parameters that, if measured experimentally, would reduce the execution mode uncertainty. We hypothesize that identifying key parameters that inform execution mechanisms could guide

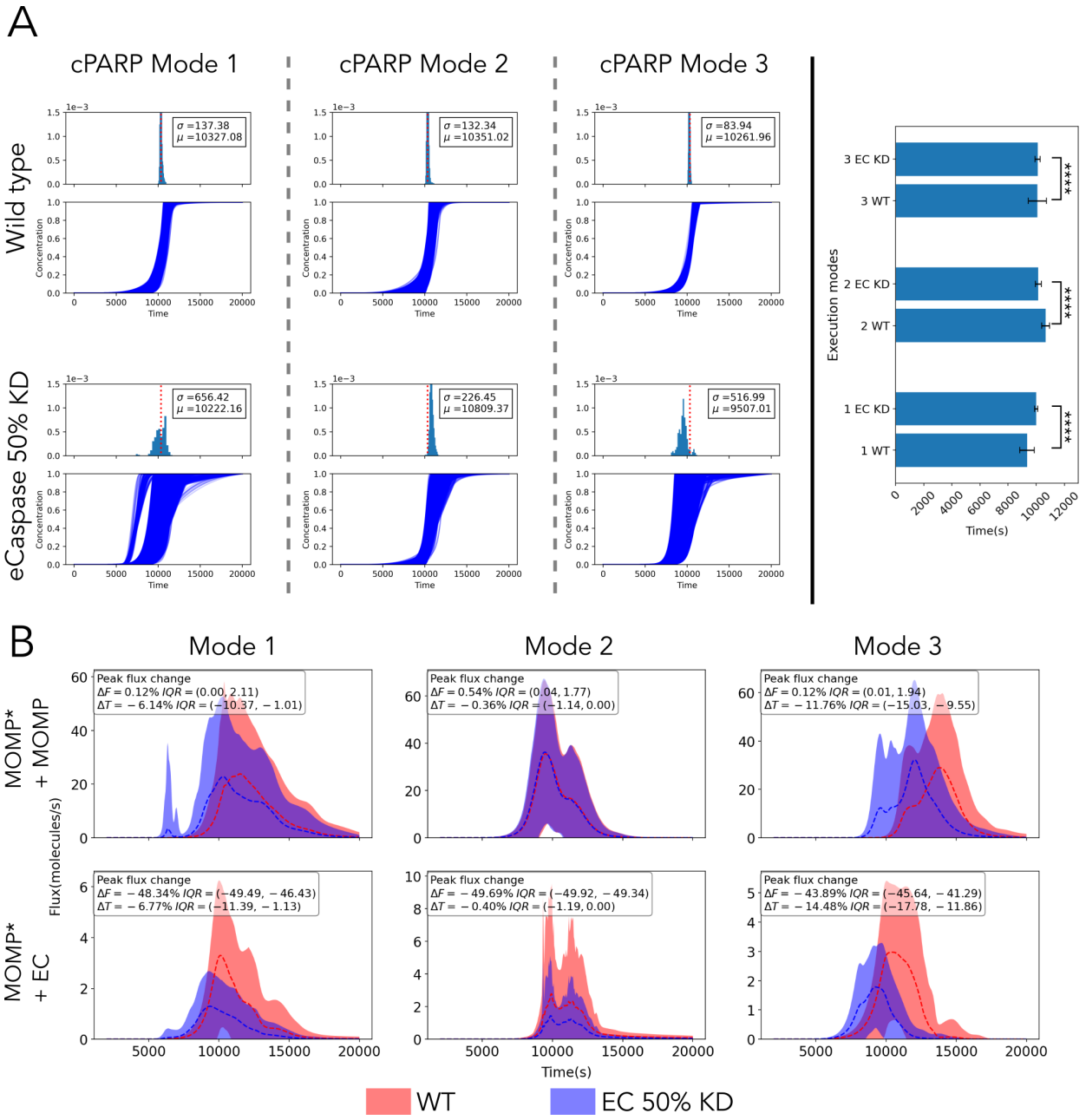

Figure 4. Time of death responses are markedly different for the same perturbation. A) Cleaved PARP (cPARP) protein concentration trajectories for the "wild type" case (top row) grouped by Execution Modes. Mode 1, 2, 3 have 11270, 10727, and 5245 trajectories, respectively. Inset includes the average time to death and the standard deviation calculated from all trajectories in each execution mode. PARP cleavage exhibits a markedly different trajectory pattern (bottom row) after eCaspase is knocked down by 50%. B) MOMP + MOMP and MOMP* + EC reaction rate trajectories. Dashed lines correspond to the mean of all reaction rates trajectories in an execution mode and the shadows represent the standard deviations. Trajectories from the "wild type" condition are colored in red and trajectories from the 50% effector caspase KD are colored in blue, and show key differences in their dynamics. Insets include the median percentage change in the reaction rate peak (ΔF) and the time to reach that peak (ΔT) in the EC KD condition relative to the wild type condition. The interquartile range is included as a measure of the variation in the ΔF and ΔT changes.*

experiments to improve our knowledge about network-driven signal processing. To measure the uncertainty of the execution modes, we used Shannon's entropy $H = -\sum_{i=1}^{n} P(x_i) \log_2 P(x_i)$ (Shannon, 1948). As aEARM has 3 execution modes the maximum entropy in the system is $\log_2 3 = 1.58$, which would signify that each execution modes have a 33% probability. Using the probabilities of the previously obtained execution modes (Figure 3A) and Shannon's formula we calculated an entropy of 1.54 indicating a high uncertainty in the execution across all modes. To determine the most informative parameters that should be measured to reduce execution mode uncertainty, we used XGBOOST (Chen and Guestrin, 2016), a gradient boosted Machine Learning technique that can classify parameter vectors into their corresponding execution modes. We used the calibrated parameter sets as training data where each individual kinetic parameter (kf, kr, kc) is a feature, and the mode of execution is our target variable.

Feature importance analysis from the XGBOOST analysis shows that parameters kf7 and kf6 contribute the most to training loss reduction during the classification task (Figure 5A). As illustrated in Figure 5C, parameters kf6 and kf7 correspond to the binding rate of MOMP* to inactivated MOMP, and MOMP* to EC, respectively. These two parameters are part of the reactions where the signal flux is bifurcated in the network, indicating that their values play an important role in the definition of the execution modes. To show the differences in parameter values for each execution mode we plotted the values of the kf6 and kf7 parameters. As shown in Figure 5B the execution modes have different distributions of the kf6 and kf7 parameters with some overlap. As depicted in Figure 5D, we simulated 100 measurements of the kf7 parameter and found that these measurements have various degrees of entropy reduction. Therefore, measuring MOMP-related parameters could help further reduce execution mode uncertainty and improve model-based predictions.

Modes of signal execution in a detailed apoptosis model with increased parameter uncertainty

Based on our results with aEARM, we then asked how a larger model with higher parameter uncertainty would fare under the presented signal execution analysis. We shifted to a larger extrinsic apoptosis reaction model (EARM V2.0), which has been studied and characterized in previous work (Lopez *et al.*, 2013). As illustrated in Figure 6A, EARMV2.0 is considerably larger than aEARM as the biochemical interactions are described with higher molecular resolution. In all, EARM V2.0 has 77 molecular species and 105 kinetic parameters. As described in Methods, we used PyDREAM to calibrate the model to published experimental data (Spencer *et al.*, 2009). Although, the calibration yielded parameter vectors that fit the experimental data indistinguishably well (supplemental Figure 4), we note that only 62 model parameters converged according to the Gelman-Rubin diagnostic (GR < 1.2) after two million iterations (see Supplemental Table 3 and Supplemental Figure 5). Distributions of 9 converged parameters are shown in Figure 6B. The remaining parameters exhibited GR values between 1.21 and 13.52 (Supplemental Table 2 and Supplemental Figure 6). From a Bayesian perspective, non-convergent parameters imply that the experimental data simply cannot constrain their values to a distribution and thus results in higher variability. As our analysis is focused on

understanding execution modes in network-driven processes, a model with poorly identified parameters presents an opportunity to explore how signal execution could be best interpreted and understood in large model systems with high parameter uncertainty.

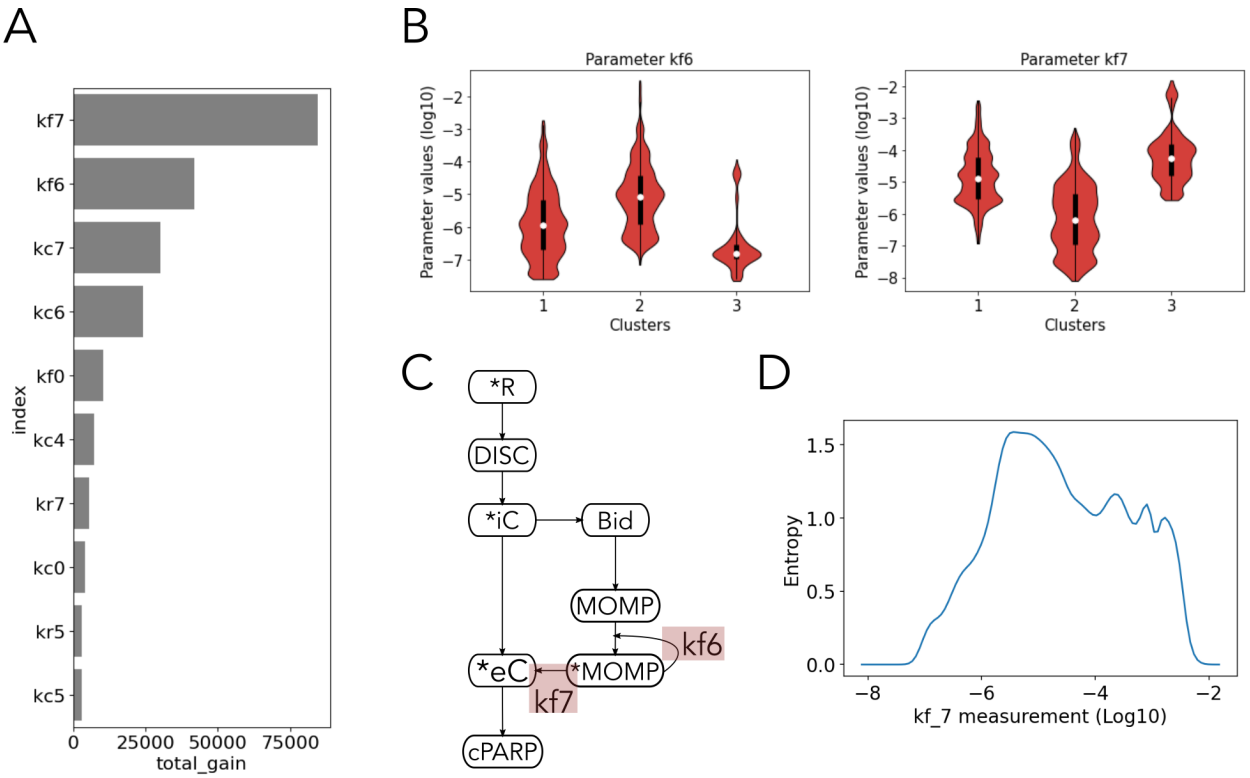

Figure 5. Parameter measurements reduce execution mode uncertainty. A) List of the 10 parameters that contribute the most to model prediction. Parameters with higher total gains, compared to another parameter, provide larger improvements to accuracy in model prediction. B) Parameter values of kf6 and kf7 grouped by the execution mode they belong to. A Gaussian kernel was used to estimate the density probability of parameter values in each execution mode. C) Schematic representation of the aEARM network. Kinetic parameters kf6 and kf7 and their corresponding reactions are highlighted in the network. D) Changes in the execution modes entropy after simulated measurements of kf7.

We followed the same procedure used in the previous sections to explore the execution modes in EARM V2.0 (See Methods for details). Our analysis found that calibration to the experimental data constrains the signal flow to eleven execution modes, that can be represented by 53 dominant subnetworks out of 2067 possible subnetworks. As shown in Figure 6C, the apoptosis execution signal could flow through any of these paths with varying degrees of probability, with Execution Mode 1 (EM1) exhibiting a probability of ~20 and the first four modes capturing ~50% of the signal probability, thus suggesting high path entropy as we have seen in previous work (Shockley *et al.*, 2019). Videos can be found in the supplement that show animations of signal flow for all execution modes in the context of EARM V2.0.

Next, we tested whether each execution mode exhibits different responses to the same perturbation. We selected EM1 and EM2 for analysis as these modes exhibit the highest probability for signal execution. As illustrated in Figure 6D, the mBid interaction with Mcl1 is dominant in EM1. In contrast, the mBid interactions with Mcl1 and Bcl2 are both dominant in EM2, thus highlighting the importance of both antiapoptotic proteins to understand the

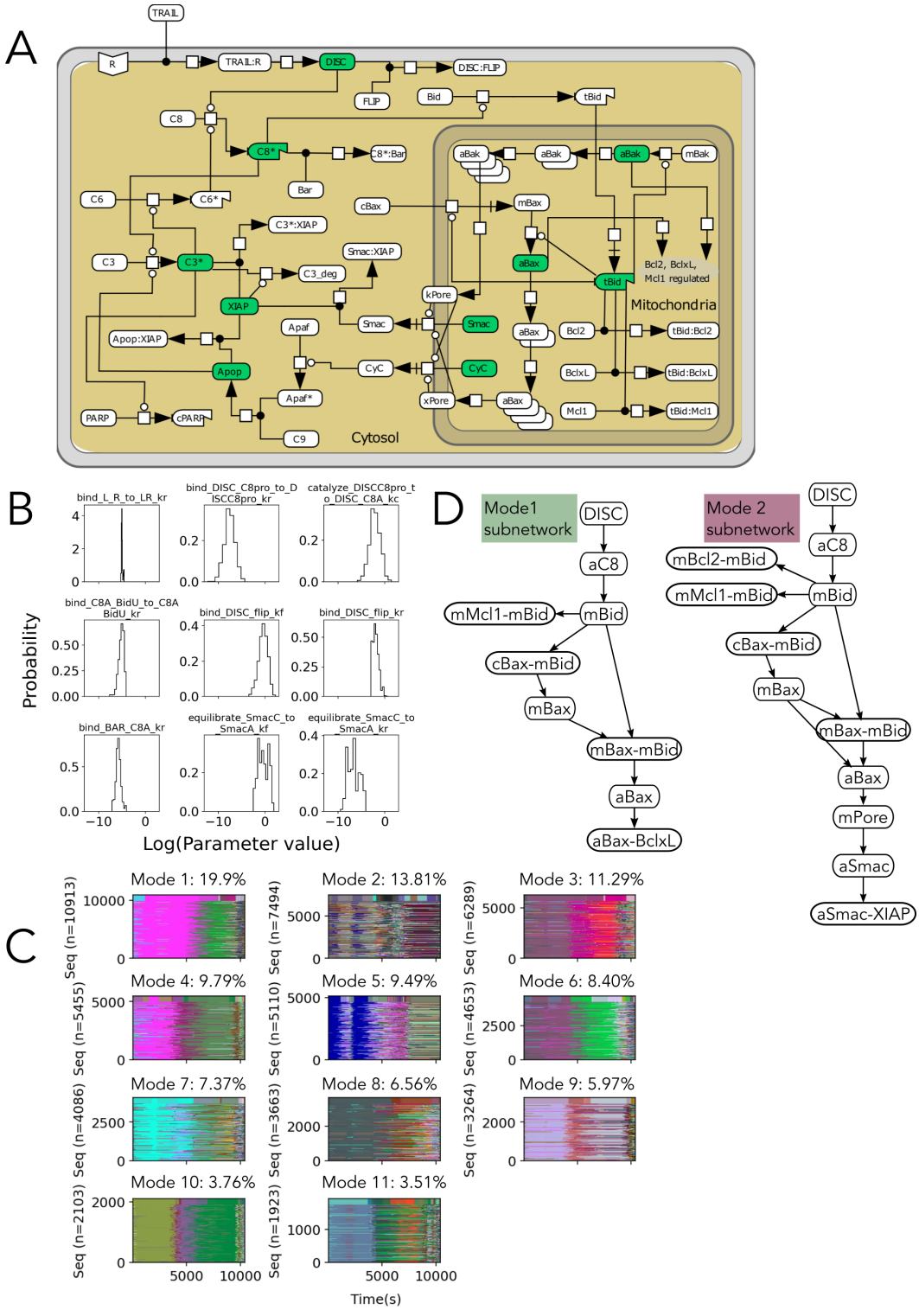

Figure 6. Modes of signal execution in the full Extrinsic Apoptosis Reaction Network. A) Network of the interactions between the proteins in the apoptosis pathway. Proteins highlighted in green are nodes where the signal flux can be divided. The convention of Kitano (Kitano *et al.*, 2005) *was followed. B) Marginal probability distributions of 9 individual kinetic parameters converged by the Gelman-Rubin diagnostic. C) Dynamic fingerprints organized by the execution modes they belong to. Each cluster plot is composed of horizontal lines that correspond to dynamic fingerprints, i.e. sequences of dominant subnetworks, and each subnetwork is assigned a different color. Execution modes are sorted from highest to lowest probability. D) Signal execution in Mode 1 (left) and Mode 2 (right) as defined by the most common subnetwork in each mode at t=7000s.*

signaling mechanisms during apoptosis execution during the cell response to an apoptotic inducer.

We then performed two *in silico experiments* for EM1 and EM2: (*i*) a 50% knockdown (KD) of the antiapoptotic protein Mcl1 as well as (*ii*) a 50% knockdown of the antiapoptotic protein Bcl2. For the Mcl1 KD, we found that the EM1 median ToD decreased from 10022.46 s (WT) to 8686.52 s (Figure 7C-upper panel). This is expected since mBid and Mcl1 interactions are dominant in this mode. By contrast the median ToD in EM2 decreased from 9943.65 s (WT) to 9335.85 s. This modest decrease in ToD can be attributed to the fact that although Mcl1 and mBid interactions are important in EM2, the dominance of Bcl2 compensates for the absence of Mcl1 and reduces the impact on ToD for the Mcl1 KD.

For the Bcl2 KD, we found that the median ToD in EM1 has a minor change from 10022.46 s to 10011.87 s, expected because mBid activity is not significantly affected by Bcl2 in this mode. By contrast, in EM2, mBid activity is modulated by Mcl1 and Bcl2. Thus, a reduction in the initial protein levels of Bcl2 enables more mBid proteins to activate pro apoptotic proteins and this leads to an increase in ToD to 9580 s (Figure 7C-upper panel). Taken together this data shows that distinct execution modes respond differently to the same perturbation and that their responses can be predicted based on the dominant reactions for a given execution mode.

To further emphasize the importance of transient dynamics on signal processing, we explored EM1 dynamic fingerprints and found that SMAC inhibition of XIAP occurs at later time points of the simulations (>8640 s). Therefore, we hypothesized that XIAP inhibition would be more effective earlier during signal execution. To test this, we added an XIAP inhibitor to EARMV2.0 at either 4000 s or 8000 s. As shown, when the inhibitor is added at the later time point, we observed a small reduction (Figure 7A lower panel) in the median ToD from 9943.65 s in the WT to 9380.44 s (Δt = 563.21 s). In contrast, when the inhibitor is added at the earlier time point, when SMAC is not yet released from the mitochondria, the inhibitor binds to XIAP enabling C3 to cleave PARP and thereby reducing the median ToD to 6766.10 (Δt = 3177.55 s).

As combination therapies have become important to combat drug resistance (Gayvert et al., 2017; Sarah, 2017), especially in cancers, we explored whether our analysis provided information about potential targets for cotreatment. As we previously mentioned, Mcl1 and XIAP are dominant antiapoptotic proteins in EM1, thus we hypothesized that inhibition of both proteins would yield a shorter ToD compared to only inhibiting XIAP. To test this, we added two drugs that independently inhibit XIAP and Mcl1 and obtained a ToD of 5951.11 s representing a 12% reduction in the ToD compared to XIAP inhibition only (Figure 7A lower panel). Finally, to guide experiments that would identify the most likely execution mode out of the 11 execution modes obtained, we developed an XGBOOST model of execution mode estimation and performed feature importance analysis. As shown in Figure 7B, we found that the parameters controlling the kinetics of mBid binding to BcxL, and XIAP binding to C3 yield the most information about execution modes in EARMV2.0. Taken together, these results suggest that the analysis of signaling dynamics from uncertain parameters help us identify dominant

reactions that control signal flow in a network during signal processing and how these networks are more sensitive to perturbations of those reactions.

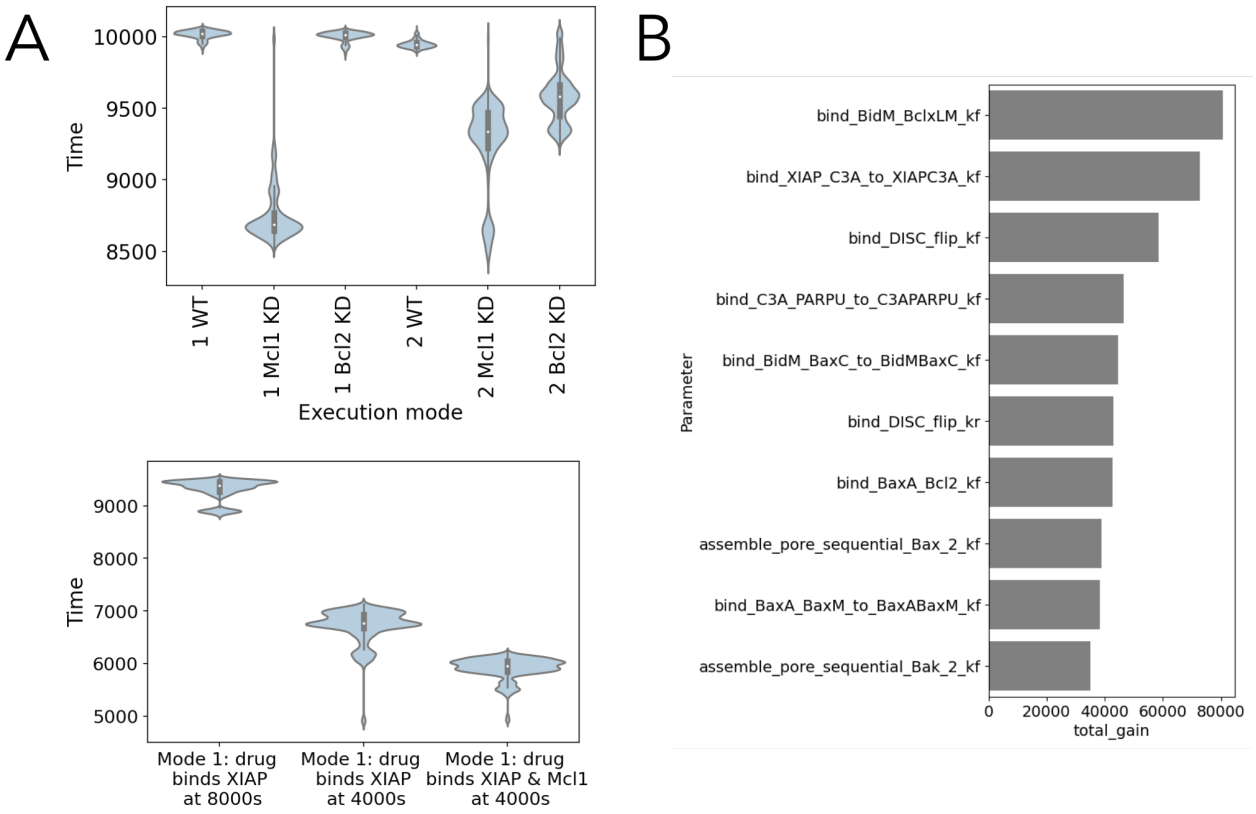

Figure 7. A) Upper panel: Time to death distributions in the execution modes 1 and 2 in the "wild type" condition, after a 50% Mcl1 knockdown, and after a 50% knockdown of Bcl2. The boxplot inside the distributions shows the median, first quartile and third quartile of the datasets. Execution modes 1 and 2 show substantial differences in their response to the knockdowns. Lower panel: Time to death distributions in the execution mode 1 after adding a drug that binds XIAP at t=8000 s, and at t=4000, and a drug that binds XIAP and Mcl1 at 4000 s. B) List of the 10 parameters in EARMv2.0 that contribute the most to model prediction.

Discussion

It has been long recognized that model parameter optimization to experimental data is key to investigate the dynamical properties that control cell behavior (Read *et al.*, 2018). Unfortunately, parameter optimization usually yields large parameter uncertainties due to a general lack of quantitative data as well as model identifiability (Ashyraliyev *et al.*, 2009). Even a complete set of time course data is insufficient to constraint most rate parameters (Ryan N. Gutenkunst *et al.*, 2007). In this work. we wanted to examine the effects of parameter uncertainty on signal execution through a biochemical network. Despite the many parameter vectors which reproduce the experimental protein dynamics, we found that the signal flow in a network was constrained to only a few modes of execution. Our analysis further shows that within a Bayesian calibration scheme, it is possible to assign probabilities to each execution mode, thus greatly improving our understanding of signal dynamics. Therefore, the probabilistic

approach introduced in this work could open a novel perspective to understand network-driven processes from a statistical perspective.

In this work we also showed that large models with high parameter uncertainty such as EARMv2.0 can be used to make model-based predictions, but those predictions should be considered within the probabilistic context provided by execution modes obtained from the calibrated parameters. Our analysis shows that parameter uncertainty as a result of model calibration can be mapped to signal execution modes that respond differently to perturbations, thus demonstrating that using a single best fit parameter vector is insufficient to understand signal dynamics in complex models. Further, our analysis allowed us to identify biochemical species, model parameters and times to maximize a given perturbation. This information about signal flow could be used to study drug-induced network rewiring processes (e.g. (Lee *et al.*, 2012)), provide mechanistic explanations to drug responses, and predict sequential combinations of drugs that could better modulate a response signal in biochemical networks.

Finally, although our approach provided novel insights about signal execution in an important biological network, it has certain limitations. Our analysis assumes that reactions with high flux are the most important for signal processing in a network. However, this may not always be the case for other networks or for networks with temporal changes in model topologies (Klinke, 2010). Although our approach is computationally expensive, particularly as models increase in size, requiring hundreds of thousands of parameter samples to reach a convergence criterion, we believe this is a relatively small price to pay in contrast to the number of experiments that would be necessary to attain the same level of mechanistic knowledge about a network-driven process.

Acknowledgements

The authors would like to thank Erin Shockley, Alexander Lubbock, Leonard Harris, Vito Quaranta, and Eric Deeds for insightful conversations and critical feedback on this work. This work was supported by the following funding sources: OOO was supported by Vanderbilt International Students Program; CFL was supported by the National Science Foundation (NSF) [MCB 1411482] and NSF CAREER Award [MCB 1942255]; and the National Institutes of Health (NIH) [U54-CA217450 and U01-CA215845].

Availability

All the code to reproduce the figures that contain model calibration, modes of signal execution, visualizations, and hypothesis exploration, is open source and can be found as Jupyter Notebooks in this GitHub repository: https://github.com/LoLab-VU/pydyno. These shareable and reusable notebooks contain all the source code and markup text that explains the rationale for each step in the analysis.

References

Albeck, J. G. *et al.* (2008) 'Modeling a Snap-Action, Variable-Delay Switch Controlling Extrinsic Cell Death', *PLoS Biology*, 6(12), p. e299. doi: 10.1371/journal.pbio.0060299.

Ashyraliyev, M. *et al.* (2009) 'Systems biology: Parameter estimation for biochemical models', *FEBS Journal*, 276(4), pp. 886–902. doi: 10.1111/j.1742-4658.2008.06844.x.

Becker, V. *et al.* (2010) 'Covering a broad dynamic range: Information processing at the erythropoietin receptor', *Science*. American Association for the Advancement of Science, 328(5984), pp. 1404–1408. doi: 10.1126/science.1184913.

Bergroth, L., Hakonen, H. and Raita, T. (2000) 'A survey of longest common subsequence algorithms', *Proceedings - 7th International Symposium on String Processing and Information Retrieval, SPIRE 2000*, pp. 39–48. doi: 10.1109/SPIRE.2000.878178.

Bonneau, R. (2008) 'Learning biological networks: From modules to dynamics', *Nature Chemical Biology*. Nature Publishing Group, 4(11), pp. 658–664. doi: 10.1038/nchembio.122.

Brennan, M. D., Cheong, R. and Levchenko, A. (2012) 'Systems biology. How information theory handles cell signaling and uncertainty.', *Science (New York, N.Y.)*, 338(6105), pp. 334–5. doi: 10.1126/science.1227946.

Campello, R. J. G. B., Moulavi, D. and Sander, J. (2013) 'Density-Based Clustering Based on Hierarchical Density Estimates', *Advances in Knowledge Discovery and Data Mining*, pp. 160–172. doi: 10.1007/978-3-642-37456-2_14.

Chen, T. and Guestrin, C. (2016) 'XGBoost: A Scalable Tree Boosting System', *Proceedings of the 22nd ACM SIGKDD International Conference on Knowledge Discovery and Data Mining*, pp. 785–794. Available at: https://doi.org/10.1145/2939672.2939785.

Cheong, R. *et al.* (2011) 'Information Transduction Capacity of Noisy Biochemical Signaling Networks', *Science*, 334(6054), pp. 354–358. doi: 10.1126/science.1204553.

Chiband, S. and Greenberg, E. (2008) 'Understanding the Metropolis-Hastings Algorithm', 49(4), pp. 327–335.

Elmore, S. (2007) 'Apoptosis: A Review of Programmed Cell Death', *Toxicologic Pathology*, 35(4), pp. 495–516. doi: 10.1080/01926230701320337.

Eydgahi, H. *et al.* (2013) 'Properties of cell death models calibrated and compared using Bayesian approaches.', *Molecular systems biology*. Nature Publishing Group, 9(644), p. 644. doi: 10.1038/msb.2012.69.

Furusawa, C. and Kaneko, K. (2012) 'A dynamical-systems view of stem cell biology', *Science*, 338(6104), pp. 215–217. doi: 10.1126/science.1224311.

Gayvert, K. M. *et al.* (2017) 'A Computational Approach for Identifying Synergistic Drug Combinations', *PLOS Computational Biology*. Edited by K. Chen. Public Library of Science, 13(1), p. e1005308. doi: 10.1371/journal.pcbi.1005308.

Gelman, A. and Rubin, D. B. (1992) 'Inference from iterative simulation using multiple

sequences', *Statistical Science*. Institute of Mathematical Statistics, 7(4), pp. 457–472. doi: 10.1214/ss/1177011136.

Gutenkunst, Ryan N. *et al.* (2007) 'Universally sloppy parameter sensitivities in systems biology models', *PLoS Computational Biology*, 3(10), pp. 1871–1878. doi: 10.1371/journal.pcbi.0030189.

Gutenkunst, Ryan N *et al.* (2007) 'Universally sloppy parameter sensitivities in systems biology models - Supporting Text 3 : Fragility of Other Predictions Fraction of Ras active Fraction of Mek active', *PLoS computational biology*, 3(10), pp. 3–4.

Harush, U. and Barzel, B. (2017) 'Dynamic patterns of information flow in complex networks', *Nature Communications*. Springer US, 8(1), pp. 1–11. doi: 10.1038/s41467-017-01916-3.

Janes, K. A. *et al.* (2005) 'Cell signaling: A systems model of signaling identifies a molecular basis set for cytokine-induced apoptosis', *Science*. American Association for the Advancement of Science, 310(5754), pp. 1646–1653. doi: 10.1126/science.1116598.

Janes, K. A., Reinhardt, H. C. and Yaffe, M. B. (2008) 'Cytokine-Induced Signaling Networks Prioritize Dynamic Range over Signal Strength', *Cell*. Elsevier, 135(2), pp. 343–354. doi: 10.1016/j.cell.2008.08.034.

Jaqaman, K. and Danuser, G. (2006) 'Linking data to models: Data regression', *Nature Reviews Molecular Cell Biology*, 7(11), pp. 813–819. doi: 10.1038/nrm2030.

Jordan, J. D., Landau, E. M. and Iyengar, R. (2000) 'Signaling networks: The origins of cellular multitasking', *Cell*, 103(2), pp. 193–200. doi: 10.1016/S0092-8674(00)00112-4.

Kantari, C. and Walczak, H. (2011) 'Caspase-8 and Bid: Caught in the act between death receptors and mitochondria', *Biochimica et Biophysica Acta (BBA) - Molecular Cell Research*, 1813(4), pp. 558–563. doi: https://doi.org/10.1016/j.bbamcr.2011.01.026.

Kato, T., Tsujimoto, S. and Zuk, A. (2017a) 'Spectral Analysis of Transition Operators, Automata Groups and Translation in BBS', *Communications in Mathematical Physics*, 350(1), pp. 205–229. doi: 10.1007/s00220-016-2702-z.

Kato, T., Tsujimoto, S. and Zuk, A. (2017b) 'Spectral Analysis of Transition Operators, Automata Groups and Translation in BBS', *Communications in Mathematical Physics*, 350(1), pp. 205–229. doi: 10.1007/s00220-016-2702-z.

Kaufmann, S. H. *et al.* (1993) 'Specific Proteolytic Cleavage of Poly(ADP-ribose) Polymerase: An Early Marker of Chemotherapy-induced Apoptosis', *Cancer Research*, 53(17), pp. 3976–3985.

Kitano, H. *et al.* (2005) 'Using process diagrams for the graphical representation of biological networks', *Nature Biotechnology*, 23(8), pp. 961–966. doi: 10.1038/nbt1111.

Klinke, D. J. (2010) 'Signal transduction networks in cancer: Quantitative parameters influence network topology', *Cancer Research*, 70(5), pp. 1773–1782. doi: 10.1158/0008-5472.CAN-09-3234.

Kochen, M. A. and Lopez, C. F. (2020) 'A Probabilistic Approach to Explore Signal Execution Mechanisms With Limited Experimental Data', *Frontiers in Genetics*, 11(July), pp. 1–17. doi:

10.3389/fgene.2020.00686.

Koonin, E. and Aravind, L. (2002) 'Origin and evolution of eukaryotic apoptosis: the bacterial connection', *Cell death and differentiation*, 9, pp. 394–404. doi: 10.1038/sj/cdd/4400991.

Lee, M. J. *et al.* (2012) 'Sequential application of anticancer drugs enhances cell death by rewiring apoptotic signaling networks', *Cell*. Elsevier Inc., 149(4), pp. 780–794. doi: 10.1016/j.cell.2012.03.031.

Levchenko, A. and Nemenman, I. (2014) 'Cellular noise and information transmission.', *Current opinion in biotechnology*. Elsevier Ltd, 28C, pp. 156–164. doi: 10.1016/j.copbio.2014.05.002.

Lopez, C. F. *et al.* (2013) 'Programming biological models in Python using PySB', *Molecular Systems Biology*. Nature Publishing Group, 9(646), pp. 1–19. doi: 10.1038/msb.2013.1.

Mehal, W. Z., Inayat, I. and Flavell, R. A. (2006) 'Caspases 3 and 7: Key Mediators of Mitochondrial Events of Apoptosis', *Science*, (February), pp. 847–851.

Mitra, E. D. and Hlavacek, W. S. (2019) 'Parameter estimation and uncertainty quantification for systems biology models', *Current Opinion in Systems Biology*. Elsevier Ltd, pp. 9–18. doi: 10.1016/j.coisb.2019.10.006.

Nobeli, I., Favia, A. D. and Thornton, J. M. (2009) 'Protein promiscuity and its implications for biotechnology', *Nature Biotechnology*, 27(2), pp. 157–167. doi: 10.1038/nbt1519.

Noel, V., Grigoriev, D. and Vakulenko, S. (2011) 'Tropical geometries and dynamics of biochemical networks . Application to hybrid cell cycle models .', pp. 1–19.

Özören, N. and El-Deiry, W. S. (2002) 'Defining characteristics of types I and II apoptotic cells in response to TRAIL', *Neoplasia*, 4(6), pp. 551–557. doi: 10.1038/sj.neo.7900270.

Perry, D. K. *et al.* (1997) 'Zinc is a potent inhibitor of the apoptotic protease, caspase-3: A novel target for zinc in the inhibition of apoptosis', *Journal of Biological Chemistry*. Elsevier, 272(30), pp. 18530–18533. doi: 10.1074/jbc.272.30.18530.

Planck, M. and Luxburg, U. Von (2006) 'A Tutorial on Spectral Clustering A Tutorial on Spectral Clustering', *Statistics and Computing*, 17(March), pp. 395–416. doi: 10.1007/s11222-007-9033-z.

Raue, A. *et al.* (2011) 'Addressing parameter identifiability by model-based experimentation', *IET Systems Biology*, 5(2), pp. 120–130. doi: 10.1049/iet-syb.2010.0061.

Read, M. N. *et al.* (2018) 'Strategies for calibrating models of biology', *Briefings in Bioinformatics*, 21(1), pp. 24–35. doi: 10.1093/bib/bby092.

Rokach, L. and Maimon, O. (2005) 'Clustering methods', *Data mining and knowledge discovery handbook*, pp. 321–352. doi: 10.1007/0-387-25465-X_15.

Sarah, C. (2017) 'Cancer: Identifying synergistic drug combinations', *Nature reviews. Drug discovery*. NLM (Medline), p. 314. doi: 10.1038/nrd.2017.76.

Shannon, C. E. (1948) 'A Mathematical Theory of Communication', *The Bell System Technical Journal*, 27(July 1928), pp. 379–423.

635 Shockley, E. M. *et al.* (2019) 'Signal integration and information transfer in an allosterically
636 regulated network', *npj Systems Biology and Applications*. Springer US, 5(1). doi:
637 10.1038/s41540-019-0100-9.

638 Shockley, E. M., Vrugt, J. A. and Lopez, C. F. (2018) 'PyDREAM: High-dimensional parameter
639 inference for biological models in python', *Bioinformatics*, 34(4), pp. 695–697. doi:
640 10.1093/bioinformatics/btx626.

641 Solania, A., González-Paéz, G. E. and Wolan, D. W. (2019) 'Selective and Rapid Cell-Permeable
642 Inhibitor of Human Caspase-3', *ACS Chemical Biology*. American Chemical Society, 14(11), pp.
643 2463–2470. doi: 10.1021/acschembio.9b00564.

644 Spencer, S. L. *et al.* (2009) 'Non-genetic origins of cell-to-cell variability in TRAIL-induced
645 apoptosis.', *Nature*. Nature Publishing Group, 459(7245), pp. 428–432. doi:
646 10.1038/nature08012.

647 Strasen, J. *et al.* (2018) 'Cell-specific responses to the cytokine TGFβ are determined by
648 variability in protein levels', *Molecular Systems Biology*, 14(1), p. e7733. doi:
649 10.15252/msb.20177733.

650 Studer, M. and Ritschard, G. (2015) 'What matters in differences between life trajectories: a
651 comparative review of sequence dissimilarity measures', *Journal of the Royal Statistical Society:
652 Series A (Statistics in Society)*, p. n/a-n/a. doi: 10.1111/rssa.12125.

653 Suderman, R. *et al.* (2017) 'Fundamental trade-offs between information flow in single cells and
654 cellular populations', *Proceedings of the National Academy of Sciences*, 114(22), pp. 5755–5760.
655 doi: 10.1073/pnas.1615660114.

656 Weerts, H. H. M., Van den Hof, P. M. J. and Dankers, A. G. (2018) 'Identifiability of linear
657 dynamic networks', *Automatica*. Elsevier Ltd, 89, pp. 247–258. doi:
658 10.1016/j.automatica.2017.12.013.

659 Yao, J., Pilko, A. and Wollman, R. (2016) 'Distinct cellular states determine calcium signaling
660 response', *MSB*, p. 92093. doi: 10.1101/059287.

661 Zhou, H. X. (2010) 'Rate theories for biologists', *Quarterly Reviews of Biophysics*. NIH Public
662 Access, 43(2), pp. 219–293. doi: 10.1017/S0033583510000120.

663